

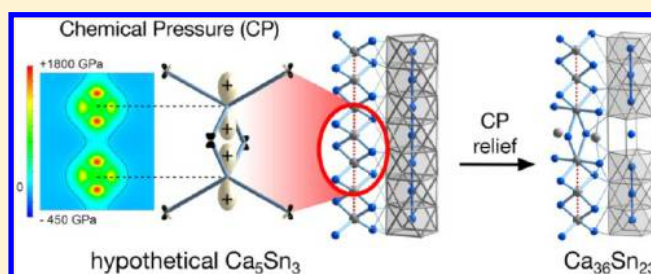
First-Principles Elucidation of Atomic Size Effects Using DFT-Chemical Pressure Analysis: Origins of $\text{Ca}_{36}\text{Sn}_{23}$'s Long-Period Superstructure

Joshua Engelkemier, Veronica M. Berns, and Daniel C. Fredrickson*

Department of Chemistry, University of Wisconsin–Madison, 1101 University Avenue, Madison, Wisconsin 53706, United States

S Supporting Information

ABSTRACT: The space requirements of atoms are empirically known to play key roles in determining structure and reactivity across compounds ranging from simple molecules to extended solid state phases. Despite the importance of this concept, the effects of atomic size on stability remain difficult to extract from quantum mechanical calculations. Recently, we outlined a quantitative yet visual and intuitive approach to the theoretical analysis of atomic size in periodic structures: the DFT-Chemical Pressure (DFT-CP) analysis. In this Article, we describe the methodological details of this DFT-CP procedure, with a particular emphasis on refinements of the method to make it useful for a wider variety of systems. A central improvement is a new integration scheme with broader applicability than our earlier Voronoi cell method: contact volume space-partitioning. In this approach, we make explicit our assumption that the pressure at each voxel is most strongly influenced by its two closest atoms. The unit cell is divided into regions corresponding to individual interatomic contacts, with each region containing all points that share the same two closest atoms. The voxel pressures within each contact region are then averaged, resulting in effective interatomic pressures. The method is illustrated through the verification of the role of Ca–Ca repulsion (deduced earlier from empirical considerations by Corbett and co-workers) in the long-period superstructure of the W_5Si_3 type exhibited by $\text{Ca}_{36}\text{Sn}_{23}$.



■ INTRODUCTION

The concept of atomic size is frequently evoked in the rationalization of experimentally observed chemical phenomena. Examples across the broad spectrum of chemistry include the nonideality of gases,¹ steric repulsion between alkyl groups influencing the outcomes of organic reactions,² the radius ratio rules for rationalizing the crystal structures of ionic salts,^{3,4} and the vibrational freedom of rattling atoms in clathrate- or skutterudite-based thermoelectric materials.^{5,6} Despite its rich history, the space requirement of atoms remains essentially an empirical notion, largely based on observed interatomic distances and the compilation of these observations in tables of atomic radii. While methods exist for partitioning space between atoms, as offered by Bader's Quantum Theory of Atoms in Molecules,^{7,8} theoretical approaches are needed for determining how a structure's stability is affected by the encroachment of one atom upon another atom's domain. Such methods would be valuable for verifying the role of atomic sizes indicated by empirical observations, and elucidating the specific ways in which these sizes wield their influence.

For solid state inorganic compounds this need is pressing, particularly for intermetallic phases. Since the pioneering work of Hume–Rothery, atomic size has been recognized as a key factor in the structural preferences of intermetallics.^{9–12} More recently, there has been an emerging theme of size effects interacting with electronic factors to determine the observed

structural chemistry.^{13–17} Investigating such interactions is quite challenging, however, as the absence of bonding schemes tying composition to geometry makes it difficult to distinguish close contacts supported by substantial bonding from those that are in fact repulsive but forced together by the constraints of atomic packing.

We recently outlined an approach for revealing local interatomic pressures that arise in such circumstances: the DFT-Chemical Pressure (CP) analysis,¹⁸ which offers theoretical insights into size effects and how they emerge from an electronic context. The DFT-CP analysis can be viewed as a chemical application of the concept of stress density,^{19–24} in which the total pressure of a system is spatially resolved into a pressure map. Our approach differs from previous work in this area in two respects. First, rather than deriving analytical relationships between the ground state wave functions and the stress density, we focus on developing a practical interface with electronic structure programs, particularly the freely available, open source ABINIT package.^{25,26} This is achieved by taking the simpler method of numerically differentiating energy density grids obtained from a calculation's output. The second difference is in our emphasis on the interpretation of the pressure maps. In moving away from considerations of the

Received: April 4, 2013

Published: May 17, 2013

formalism of stress densities toward visualization of the conflicts underlying them, vivid schemes for the stability of intermetallic structures arise that are capable of inspiring new experimental endeavors.

In this Article, we build on our earlier outline of the DFT-CP analysis. In the process of describing the methodological details of this approach, we will present improvements that develop the DFT-CP analysis into a generally usable tool for the analysis of bonding optimization in solid state materials. These improvements include a more meaningful treatment of the pressures observed in the regions of the ion cores and a more reliable method for dividing space between the atoms during the integration of the pressure maps. In addition, we will demonstrate the application of this improved analysis to an intermetallic system with interesting structural chemistry: that of the superstructure variants of the W_5Si_3 structure type in the Ca–Sn system.

■ OUR MODEL SYSTEM

As we develop the DFT-CP method in this Article, we will use the complex crystal structure of $Ca_{36}Sn_{23}$ (Figure 1) as a model

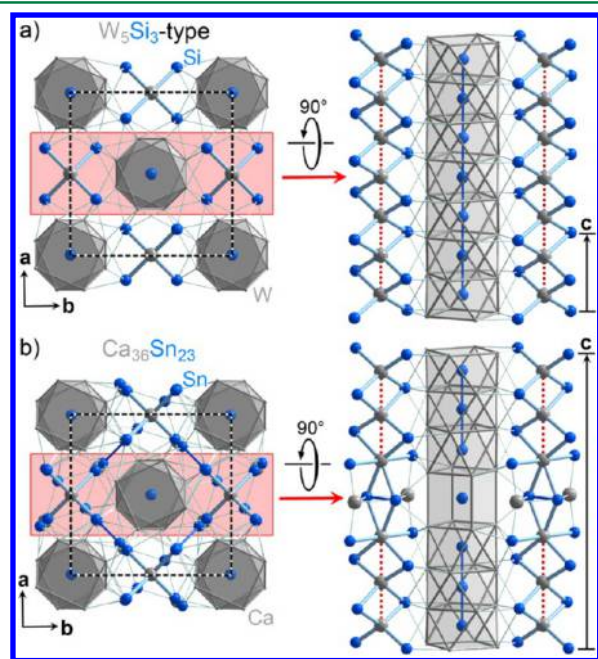


Figure 1. The crystal structure of $Ca_{36}Sn_{23}$, whose stability has been attributed to the Ca–Ca repulsion that would occur in its W_5Si_3 -type parent structure. (a) The structure of W_5Si_3 . (b) The $Ca_{36}Sn_{23}$ structure, which is generated through the introduction of planar defects into the W_5Si_3 -type at regular intervals perpendicular to c .

system.^{27,28} This compound belongs to a family of intermetallics adopting long-period superstructures of the common W_5Si_3 structure type (Figure 1a).^{27–34} The W_5Si_3 parent structure is easily visualized as a checkerboard arrangement of columns of Si-centered W square antiprisms and columns of W-centered Si tetrahedra. These two column types extend along the c -axis, with the square antiprisms and tetrahedra of each column linked through shared faces and edges, respectively.

In $Ca_{36}Sn_{23}$ and a number of other phases, defect variants of the W_5Si_3 type are adopted in which planar interfaces are inserted perpendicular to c (as shown on the right side of

Figure 1b). At each of these interfaces, the progression along the columns of square antiprisms is interrupted by the incorporation of a cube. The columns of tetrahedra are similarly interrupted, with the coordination of the interfacial Ca atoms changing from tetrahedral to octahedral. In $Ca_{36}Sn_{23}$, these interfaces occur at regular intervals of six square-antiprisms along c , corresponding to three unit cells of the W_5Si_3 basic structure. For other members of this family, other interface distributions are observed (Figure 2). In the structures of $Ca_{31}Sn_{20}$ and $Pu_{31}Pt_{20}$, the interface layers are separated from each other by slabs of the W_5Si_3 type five square antiprisms thick. For Y_3Rh_2 and Ca_6Sb_{11} , the slab thickness decreases to respectively three and two square antiprisms.

The gradual shrinking of the W_5Si_3 -type domains across this series is an impressive illustration of the structural flexibility obtained in intermetallic phases and raises the question of what driving forces motivate such progressions. For this particular series, Corbett and co-workers have provided a plausible explanation for the instability of the simple W_5Si_3 type in, for instance, the Ca–Sn system: in a hypothetical Ca_5Sn_3 phase, the neighboring Ca atoms in the tetrahedral chains would be expected to have unusually short distances to each other (3.3 Å, by our estimation; see Figure 3), suggesting that the Ca atoms may be too large for their coordination environment.³⁴ The interfaces in the observed superstructures in this series could serve to alleviate interatomic repulsion at such contacts.

Atomic size thus appears to be playing a part in the structural series of Figure 2. How might electronic structure calculations be used to support and inform this view? Over the course of this paper, we will see that the DFT-Chemical Pressure analysis provides a first-principles approach to this problem, which reveals in graphical and intuitive terms not only the Ca–Ca repulsion in a hypothetical W_5Si_3 -type basic structure but also its release upon moving to the observed $Ca_{36}Sn_{23}$ structure. A first step will be introducing some improvements to the original DFT-CP scheme described earlier, which makes the method more amenable to systems with atoms of very different sizes and valence electron counts.

■ COMPUTATIONAL PROCEDURES

For all calculations on $Ca_{36}Sn_{23}$ and a hypothetical W_5Si_3 -type Ca_5Sn_3 phase, two planewave-based DFT codes were used because of their complementary strengths. The Vienna Ab initio Simulation Package (VASP)^{35,36} was used for the geometrical optimization of the two structures due to the highly efficient potentials provided with the package, requiring relatively low energy cut-offs. The geometrical optimizations were performed in two steps: first the ion positions were optimized within a unit cell of fixed dimensions, then all structural parameters were optimized simultaneously. All calculations used the local-density approximation (LDA) and were carried out in the high precision mode, corresponding to an energy cutoff of 106.4 eV. The calculations employed $4 \times 4 \times 8$ and $4 \times 4 \times 2$ Monkhorst-Pack k -point meshes³⁷ for Ca_5Sn_3 and $Ca_{36}Sn_{23}$, respectively, and the ultrasoft pseudopotentials provided with the package.³⁸

The ABINIT package^{25,26} was used for generating the necessary data for the DFT-CP analysis of the VASP-optimized structures, because of the exquisite degree of detail and transparency in its output. For each structure, the raw data for the CP analysis was obtained through three single-point calculations spanning a volume range of 0.6%. The calculations employed the LDA exchange-correlation functional of

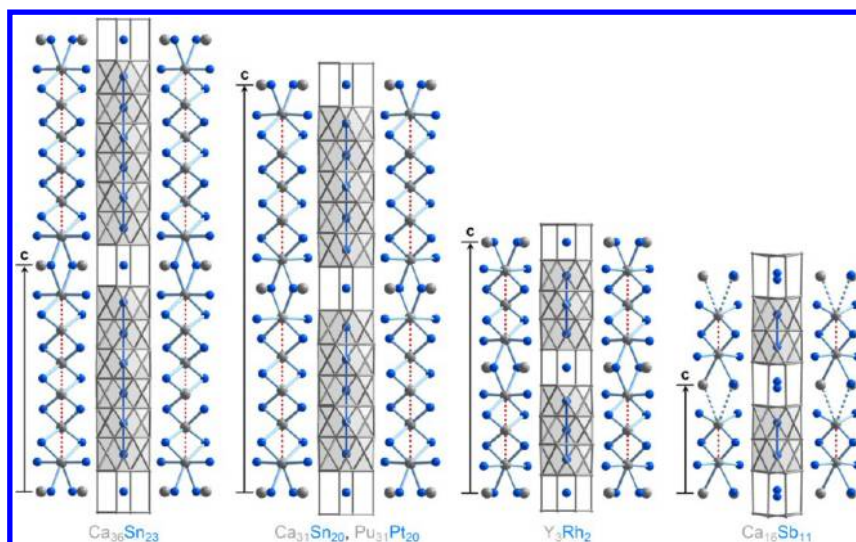


Figure 2. A family of long-period superstructures of the W_5Si_3 type with regularly spaced planar interfaces perpendicular to c .

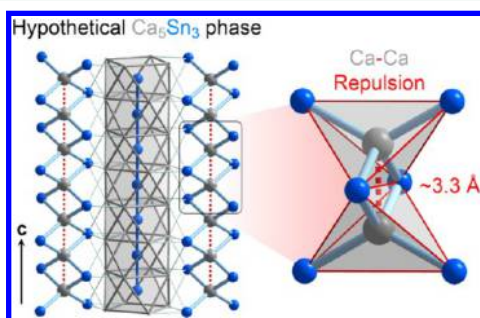


Figure 3. The model of Corbett et al. for the instability of the W_5Si_3 -type structures in phases with large electropositive atoms at the W-type positions, illustrated with Ca_5Sn_3 . The placement of Ca in the edge-sharing tetrahedral chains running along c leads to uncomfortably close Ca–Ca contacts. The superstructures of the W_5Si_3 type observed in these systems are hypothesized to relieve interatomic repulsion at these contacts.

Goedecker, Teter, and Hutter³⁹ and the Hartwigsen-Goedecker-Hutter (HGH) pseudopotentials provided with the package.⁴⁰ The energy cutoff was set to 816 eV for the calculations on $Ca_{36}Sn_{23}$ and Ca_5Sn_3 when the valence-only Ca HGH potential was used. For Ca_5Sn_3 , calculations were also carried out using the semicore Ca HGH potential; here the energy cutoff was set to 1088 eV. These values were found to converge the energy of formation of the hypothetical Ca_5Sn_3 phase to less than 0.5 meV/atom. Monkhorst-Pack k-point meshes³⁷ distributing $4 \times 4 \times 2$ and $4 \times 4 \times 8$ points through the Brillouin zone were used for the $Ca_{36}Sn_{23}$ -type and W_5Si_3 -type phases, respectively. The spacing of the voxels (determined by the fast Fourier transform grids) was set to $108 \times 108 \times 192$ and $108 \times 108 \times 72$ grids for $Ca_{36}Sn_{23}$ and Ca_5Sn_3 , respectively. Cross-sections of the CP maps were plotted with the program VESTA 3.⁴¹

■ CREATING CHEMICAL PRESSURE MAPS

To set up the discussion of our improvements to the DFT-Chemical Pressure (CP) scheme and its application to $Ca_{36}Sn_{23}$, let us briefly review the method. The basis of the DFT-CP analysis is the electronic packing frustration model (Figure 4) for the interplay between electronic interactions and

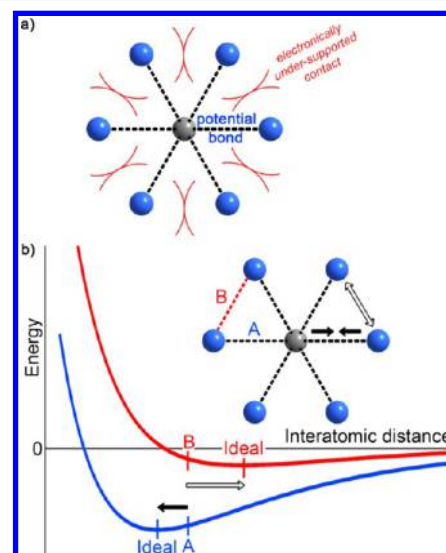


Figure 4. Nonideal interatomic distances and local chemical pressures resulting from electronic packing frustration (EPF). (a) A schematic illustration of the electronic packing frustration model. Reproduced from ref 42 with the kind permission of the American Chemical Society. (b) The compromise between the need for contraction along some contacts (A) and expansion along others (B) leads to nonoptimal distances. The slope of an energy vs distance curve at the observed distance is related to a local pressure acting at that contact.

atomic size in condensed matter systems.^{42,43} Dense atomic packing constraints can lead to correlations between interatomic distances within a structure. Such correlations make it difficult to independently optimize the interactions between different pairs of atoms. The size of atoms becomes manifest when the formation of a chemical bond at one contact requires shortening at other contacts for which there is not sufficient electronic support. Such tension would be expected to result in nonoptimal interatomic distances (Figure 4b) and local pressures acting between the affected atoms, which might be referred to with the term *chemical pressure* (CP) to distinguish them from physical pressures exerted on the system externally.

The formalism of the quantum mechanical stress density^{19–23} offers one approach for determining how such pressures are distributed in a crystal structure. In the DFT-CP analysis, a simpler avenue is taken, in which the structure is divided into a grid of voxels (small finite volume elements) and the pressure experienced by each voxel is calculated as follows.

We begin with the expression for the total energy for a system calculated with Kohn–Sham DFT:⁴⁴

$$E_{\text{total}} = \iiint_{\text{unit cell}} \left(\sum_n -\frac{\partial_n}{2} \psi_n^* \nabla^2 \psi_n + \left(V_{\text{local}} + \frac{1}{2} V_{\text{Hartree}} + \varepsilon_{\text{XC}}(\rho) \right) \rho(\vec{r}) \right) dV + E_{\text{Ewald}} + E_{\text{nonlocal}} + E_{\alpha} \quad (1)$$

In this expression, the terms under the integral represent the kinetic energy of the system and the local contributions to the potential energy, measured relative to the reference state of an exchange-correlation-free homogeneous electron gas interacting with the ion cores. Outside the integral, the $E_{\text{Ewald}} + E_{\alpha}$ terms together give the energy of that reference state, and E_{nonlocal} provides the potential energy resulting from any nonlocal components of the atomic pseudopotentials (an additional term $E_{\text{KT-Entropy}}$ can be added to correct the total energy from any smearing of the band occupancies about the Fermi energy).

The next step in the determination of the DFT-CP distribution is to recognize that the E_{total} expression has the form of the integral over an energy density plus a remainder:

$$E_{\text{total}} = \iiint_{\text{unit cell}} \rho_{\text{energy}}(\vec{r}) dV + E_{\text{remainder}} \quad (2)$$

which can be represented more conveniently for numerical work as a sum over a grid of voxel energies plus a remainder:

$$\begin{aligned} E_{\text{total}} &\approx \sum_n^{N_{\text{voxels}}} \rho_{\text{energy}}(\vec{r}) V_{\text{voxel}} + E_{\text{remainder}} \\ &\approx \sum_n^{N_{\text{voxels}}} E_{\text{voxel},n} + E_{\text{remainder}} \end{aligned} \quad (3)$$

where N_{voxels} is the number of voxels into which the unit cell volume (V_{cell}) is divided, and V_{voxel} is the volume of each voxel, i.e. $V_{\text{voxel}} = V_{\text{cell}}/N_{\text{voxels}}$.

Once the total energy is mapped spatially in this way, a similar spatial distribution of the pressure is obtained by taking the negative derivative of E_{total} with respect to V_{cell} :

$$\begin{aligned} P &= -\frac{\partial E_{\text{total}}}{\partial V_{\text{cell}}} = -\frac{\partial}{\partial V_{\text{cell}}} \left(\sum_n^{N_{\text{voxels}}} E_{\text{voxel},n} + E_{\text{remainder}} \right) \\ &= -\frac{\partial}{\partial V_{\text{cell}}} \left(\sum_n^{N_{\text{voxels}}} E_{\text{voxel},n} \right) + P_{\text{remainder}} \\ &= -\frac{1}{N_{\text{voxels}}} \left(\sum_n^{N_{\text{voxels}}} \frac{\partial E_{\text{voxel},n}}{\partial V_{\text{voxel}}} \right) + P_{\text{remainder}} \\ &= \frac{1}{N_{\text{voxels}}} \sum_n^{N_{\text{voxels}}} P_{\text{voxel},n} + P_{\text{remainder}} \end{aligned} \quad (4)$$

so that the total pressure experienced by the structure, P , becomes resolved into an average over the voxel pressures ($P_{\text{voxel},n}$) plus a remainder pressure arising from components of the total energy that are not easily mapped spatially.⁴⁵ In practice, this differentiation is performed numerically by constructing energy grids from the output of ABINIT calculations^{25,26} on a structure at two slightly different volumes, taking the difference, and dividing by the difference in voxel volumes.

How should the $P_{\text{remainder}}$ term be treated? In Section S1 of the Supporting Information, we describe how in principle the pressure contributions from E_{Ewald} , E_{α} and E_{nonlocal} can be apportioned among the atoms or interatomic regions of the structure. However, in each case, one encounters an unacceptable degree of ambiguity in applying the procedure which leads to unreliable results. Through work with several intermetallic systems, we have concluded that the best treatment of $P_{\text{remainder}}$ is also the simplest: we consider it as corresponding to a homogeneous background pressure, which can then be added to each of the voxel pressures.

For metallic phases lacking localized bonds, the pressure grids resulting from this procedure tend to have high-magnitude features near the nuclear positions, occurring in the midst of a relatively flat negative background pressure. This is illustrated for a hypothetical W_5Si_3 -type phase Ca_5Sn_3 (the parent structure of the more complex $\text{Ca}_{36}\text{Sn}_{23}$ structure we discussed above) in Figure 5a. Here, cross sections of the CP

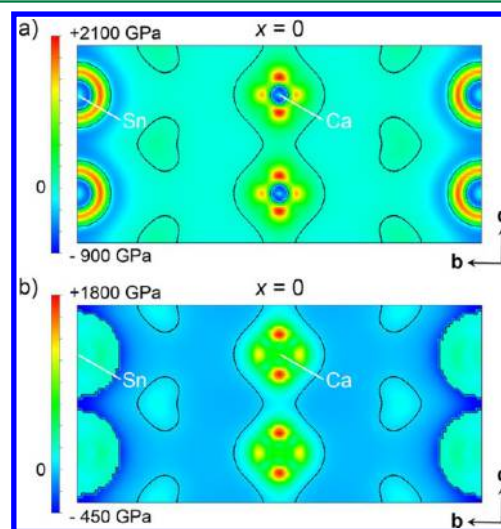


Figure 5. Cross sections of the chemical pressure (CP) map of a hypothetical W_5Si_3 -type Ca_5Sn_3 , taken through the $x = 0$ plane. The cross sections are shown (a) before and (b) after flattening of the spherically symmetric oscillations emanating from the ion cores. Black contours corresponding to $\text{CP} = 0$ are overlaid on the map. See text for details.

map are taken perpendicular to the a -axis and centered on the unusually close Ca–Ca contacts. The pressures in the map are indicated using colors ranging from dark blue (–900 GPa) to red (+2100 GPa). The most vivid variations in color occur near the nuclear positions, where negative pressures at the atom centers give way to intense positive pressures slightly further out, arranged in a ring for the Sn and in a cross for the Ca. As the distance from the nuclei increases, the voxel pressures gradually converge on a relatively flat background pressure.

■ ISOTROPIC CORE COMPONENT AVERAGING

The presence of strong CP oscillations emanating from the ion cores poses a number of problems for the interpretation of the CP maps. First, the magnitudes of the pressures encountered during these undulations dwarf those appearing in the interatomic regions of the map. This makes more subtle features of the map difficult to detect. A second undesirable aspect of these oscillations is that they tend to mask any directional dependence of the pressures in the core region, as might emerge from an interatomic interaction. Finally, as the core region contains both large positive and negative pressures, it is difficult to gauge the net pressure near the nucleus. As we are using pseudopotentials, the question of how seriously to take these oscillations is important. They occur largely in the pseudopotential core regions, where the correspondence is weakest between the true wave functions of the system and the pseudowave functions of the calculation. In other words, their specific forms are artificial products of the atomic pseudopotentials.

The form of the pseudopotential near the core is typically chosen to be mathematically convenient while still reproducing key atomic properties. Likewise, we can substitute the oscillatory CP features with a simpler CP distribution that captures the same net pressure and directional dependence upon integration over the core region. In order to accomplish this, we have developed an *isotropic core component averaging* procedure for use in the generation of DFT-CP maps.

We begin by choosing a radius for the core region of an atom, typically about 1.0 Å. The voxels within this distance of the nuclear position will be subject to this procedure, while all others will be left unchanged. Next, the pressure for any voxel in the core region, say the n th voxel in the grid, is written in terms of its deviation from the average P for that voxel's distance from the nucleus, $r_{n-ion} = |\vec{r}_{voxel,n} - \vec{R}_{ion}|$:

$$\begin{aligned} P_{voxel,n} &= [P_{voxel,n} - \overline{P_{voxel}(r_{n-ion})}] + \overline{P_{voxel}(r_{n-ion})} \\ &= \Delta P_{voxel,n} + \overline{P_{voxel}(r_{n-ion})} \end{aligned} \quad (5)$$

In other words, the core voxel pressures are written as the sum of an anisotropic function, representing the directional dependence of the core pressures, and a spherically symmetric function.

The oscillations around the core occur predominantly in the latter function, the isotropic core component. These can be removed by simply replacing the values of this function with its average within the core region:

$$P_{core}^{isotropic} = \frac{\int_0^{r_{core}} \overline{P_{voxel}(r_{n-ion})} \cdot 4\pi(\vec{r}_{n-ion})^2 dr_{n-ion}}{\frac{4}{3}\pi r_{core}^3} \quad (6)$$

In this way, the modified voxel pressures are calculated as

$$P_{voxel,n} = \Delta P_{voxel,n} + P_{core}^{isotropic} \quad (7)$$

Under this transformation, both the anisotropic component and the average of the isotropic function are left unchanged. As such, the net pressure within the core region and the directional dependence are preserved.

In Figure 5b, we replot the DFT-CP cross-section of the hypothetical Ca_5Sn_3 structure through the $x = 0$ layer, this time with the isotropic core component averaging applied with core radii of 0.8 Å for Ca and 1.3 Å for Sn. For both atom types,

there is significant reduction in the variation of pressures in the core region. In the case of Sn, the ripples of color are now replaced with a virtually uniform cyan, corresponding to a slightly positive pressure, distributed over large circles with pixilated edges. This pixilation marks the discontinuous change in the CP distribution upon leaving the averaged core region. This offers a much more straightforward view of the Sn's core pressures than the untreated CP map of Figure 5a: the Sn cores have net positive pressures which are essentially isotropic.

The Ca cores in this plot become similarly smoother. Upon averaging over the spherically symmetric components, the blue cores at the atom centers disappear, yielding a distribution that is uniformly positive. A highly anisotropic character to the Ca core also becomes more apparent. Red spots appear just above and below the Ca nuclear pressures, indicating colossal positive pressures of 1800 GPa. These positive CP features lie along the unusually short Ca–Ca contacts of the structure (2.96 Å in our LDA-DFT optimized geometry), to which Corbett and co-workers attributed the nonexistence of this compound. This is the first of several indications we will see in the DFT-CP analysis of this system of the truly repulsive nature of the interactions at these contacts.

Another difference between the CP maps of Figures 5a and 5b is notable. Upon removing the oscillatory character of the core pressures, the pressure range seen in the structure shrinks from 3000 GPa down to 2250 GPa. This 750 GPa reduction in the pressure range captured by the color map allows for a greater contrast between features in the space outside of the cores, although in this case the repulsive character of the Ca–Ca contacts remains the most striking aspect of the map.

■ INTEGRATION AND PROJECTIONS OF THE CP DISTRIBUTION AROUND ATOMS

The results of the isotropic core component averaging described in the last section reinforce the view of the CP distribution as consisting of core regions with net positive pressure immersed in a background of negative pressure. Interpreting the overall pressure exerted by the interatomic contacts on each atom then requires an integration of the pressure map and its directionality around the atom's position.

The angular dependence of the pressure distribution surrounding an atom plays a central role here. Because of this, we will now describe in detail our procedure for determining the pressures experienced by the atoms along different directions. This process begins with a projection of the CP distribution onto spherical harmonics as follows

$$a_{lm} = \frac{1}{N_{voxels,atom}} \sum_n w_{n,atom} P_{voxel,n} Y_{l,m}(\theta_n, \phi_n) \quad (8)$$

where $w_{n,atom}$ is the fraction of voxel n 's pressure that is attributed to the atom in question, $N_{voxels,atom} = \sum_n w_{n,atom}$ is the number of voxels belonging to the atom, and (θ_n, ϕ_n) are the angular components of the spherical polar coordinates of voxel n with the origin being the atom's nucleus. The projections a_{lm} can be used to reconstruct this angular distribution—or the chemical pressure anisotropy, $CP_{aniso}(\theta, \phi)$, of the atom—where all pressure contributions are now mapped onto the unit sphere

$$CP_{aniso}(\theta, \phi) = \sum_{l \leq l_{max}} \left(\sum_{-l \leq m \leq l} a_{lm} Y_{l,m}(\theta, \phi) \right) \quad (9)$$

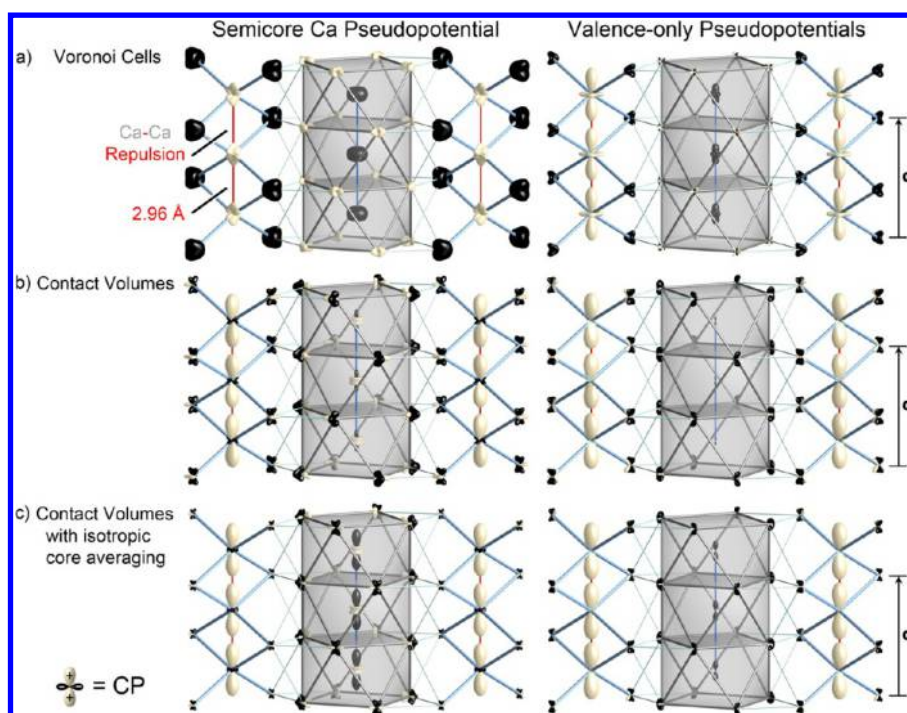


Figure 6. The dependence of the chemical pressure (CP) anisotropies of atoms in the hypothetical Ca_5Sn_3 structure on the method of dividing voxels among the atoms, employing Ca pseudopotentials treating semicore electrons explicitly (left column) and as part of the pseudopotential core (right column). The CP distribution around each atom is shown as a radial plot, with the distance between the atom's nucleus and a point on the surface being proportional to the pressure magnitude along that direction. The color of the surface indicates the sign of the pressure: black for negative, white for positive. The plots are shown for results obtained when (a) dividing space into the Voronoi cells of the atoms, (b) dividing space into contact volumes, within which the distributions are averaged before carrying out the projections, and (c) applying the contact volume scheme to a CP map that has undergone isotropic core component averaging. The final method yields the greatest agreement between the two calculations using different models for the Ca core. The scales of the CP surfaces in the various panels are chosen for maximum clarity rather than consistency.

with l_{\max} being the l index of the highest order spherical harmonics to be included in the projection.

The interpretation of this function is made clear by taking a closer look at the a_{00} coefficient. As $Y_{0,0} = 1/(4\pi)^{1/2}$, a_{00} is simply calculated as

$$a_{00} = \frac{1}{N_{\text{voxels},\text{atom}}} \sum_n w_{n,\text{atom}} P_{\text{voxel},n} \sqrt{\frac{1}{4\pi}} = P_{\text{atom}} \sqrt{\frac{1}{4\pi}} \quad (10)$$

where P_{atom} is the nominal average pressure experienced by the atom. The summation of terms giving rise to the $CP_{\text{aniso}}(\theta, \phi)$ function then begins as

$$CP_{\text{aniso}}(\theta, \phi) = P_{\text{atom}} \sqrt{\frac{1}{4\pi}} \cdot \sqrt{\frac{1}{4\pi}} + \dots = \frac{P_{\text{atom}}}{4\pi} + \dots \quad (11)$$

In this way, the higher order terms describe how the CP anisotropy function differs from a sphere whose radius is proportional to the average pressure of the atom.

The role of the $1/4\pi$ factor in eq 11 can be understood by taking the integral of the function over the unit sphere. In this case all of the higher-order terms integrate to zero, and we are left with

$$\begin{aligned} & \int_{\phi=0}^{\phi=2\pi} \int_{\theta=0}^{\theta=2\pi} \sin(\theta) CP_{\text{aniso}}(\theta, \phi) d\theta d\phi \\ &= \int_{\phi=0}^{\phi=2\pi} \int_{\theta=0}^{\theta=2\pi} \sin(\theta) \frac{P_{\text{atom}}}{4\pi} d\theta d\phi \\ &= \frac{P_{\text{atom}}}{4\pi} \int_{\phi=0}^{\phi=2\pi} \int_{\theta=0}^{\theta=2\pi} \sin(\theta) d\theta d\phi = P_{\text{atom}} \end{aligned} \quad (12)$$

The integral thus recovers the average pressure for the atom. The factor $\sin(\theta)d\theta d\phi/4\pi$ can then be thought of as a weight in averaging over the sphere.

We now arrive at a straightforward means of interpreting the numerical values of the $CP_{\text{aniso}}(\theta, \phi)$ function: Multiplying the function by 4π yields the net pressure experienced along each direction, $P_{\text{atom}}(\theta, \phi)$, i.e.

$$P_{\text{atom}}(\theta, \phi) = 4\pi \cdot CP_{\text{aniso}}(\theta, \phi) \quad (13)$$

$$P_{\text{atom}} = \overline{P_{\text{atom}}(\theta, \phi)} = \int_{\phi=0}^{\phi=2\pi} \int_{\theta=0}^{\theta=2\pi} P_{\text{atom}}(\theta, \phi) \frac{\sin(\theta) d\theta d\phi}{4\pi} \quad (14)$$

Once the $P_{\text{atom}}(\theta, \phi)$ function is calculated, it can be easily represented graphically using radial plots, as in Figure 6. In these images, a CP surface is plotted on each atom, with the distance of the atom to a point on the surface with coordinates (θ, ϕ) being proportional to the magnitude of the CP

experienced along that direction. The signs of the pressures are given by the color of the surface. Black features in the plots correspond to directions along which contraction is favorable (evoking the image of a black hole pulling inward on its surroundings). Lobes in white indicate directions for which expansion is desired (by analogy with the bright radiance of white hot stars).

There are two parameters involved in the creation of such plots: the l_{\max} value and the form of the weighting scheme leading to the $w_{n,\text{atom}}$ values. l_{\max} simply determines to what detail the angular distributions of the CP map is captured. From our experience, setting l_{\max} beyond 4 or 5 substantially increases the processing time without leading to any significant changes in the qualitative pressure schemes. For this reason, we use 4 here for the upper limit. The selection of the scheme for distributing the voxel pressures among the atoms is a more involved issue and is the focus of the next section.

■ THE CONTACT VOLUME INTEGRATION SCHEME

In the projections of the CP map described above, a key parameter is the way in which the structure is divided among the atoms. For the Sr–Ag and Ca–Ag structures we examined earlier,¹⁸ we tested several schemes for this, including the use of fixed spheres around the atomic positions, the division of space into Voronoi cells⁴⁶ ($w_{n,\text{atom}} = 1$ if voxel n is within the Voronoi cell of the atom), and the atomic domains revealed through the use of Bader's Quantum Theory of Atoms in Molecules.^{7,8} For these cases, the Voronoi cell approach provided results that were easiest to interpret, in that the CP surfaces on pairs of atoms agreed most closely in their signs and magnitudes along the vector separating them. Unresolved is whether the Voronoi scheme works in all cases and, if not, what would provide a more robust partitioning of space.

In Figure 6a, we explore this question by showing CP anisotropy surfaces calculated for a W_5Si_3 -type Ca_5Sn_3 phase, the hypothetical parent to the complex $\text{Ca}_{36}\text{Sn}_{23}$ structure, integrated with the Voronoi scheme. The results are shown using two Hartswigen-Goedecker-Hutter pseudopotentials for Ca available with the ABINIT package, to explore how stable the CP picture is to changes in the modeling of the core regions of the atoms. The calculation leading to the image in the left panel employed the semicore Ca potential, in which the usual Ca $4s^2$ set of valence electrons is expanded to include lower energy $3p^6$ and $3s^2$ electrons, for a total of 10 valence electrons/Ca atom. The right panel shows the result using the valence-only potential, in which just the Ca $4s^2$ electrons are considered explicitly.

Similarities and differences between the two plots occur. In both cases, the surfaces on the tetrahedrally coordinated Ca atoms exhibit white lobes pointing across the shared tetrahedral atoms toward their Ca neighbors. This indicates that positive, repulsive pressures occur at these contacts, as is consistent with the unusually short Ca–Ca distances here (2.94 Å in our LDA-DFT optimized structures). However, the shapes of these calcium CP surfaces differ dramatically. For the Ca semicore calculation, triangular positive pressure lobes, resembling the bodies of squid, point toward the neighboring Ca atoms. In the valence-only Ca result, long, nearly cylindrically symmetric lobes appear at these places instead. Additional positive pressure features occur around the equator of the CP anisotropy surfaces.

The remaining features in the plot are more difficult to interpret. The Sn atoms appear with black bulbous surfaces, but

whose relative sizes and shapes vary between the two plots. For the two results a similar story emerges of Ca–Ca repulsion against a backdrop of the other interactions, but the inconsistencies indicate that the Voronoi approach is rather sensitive to the details of the treatment of the core region.

A more basic drawback of using the Voronoi approach in this system can be seen by beginning with points on the black Sn surfaces in either image and following some of these directions toward the neighboring Ca atoms. In many cases the black Sn surfaces point to white features on Ca surfaces. Along the Ca–Sn contacts, then, we see desires for contraction on the Sn and for expansion on the Ca. Missing here is an immediate answer to the issue of whether these Ca–Sn contact distances are too long or too short.

Unlike the Ca–Ag and Sr–Ag structures we examined earlier, it appears that drawing boundaries between atomic cells at the midpoints between contacts is too crude of an assumption for this system. One could imagine moving the boundaries back and forth to make the atomic cells better reflect the relative sizes of the atoms. Such a procedure is included in our latest version of the *CPintegrate* program, using the additively weighted Voronoi method.⁴⁶ We have found, however, that this approach is of limited use, particularly when examining combinations of atoms with very different numbers of core-like electrons in their valence sets.

A first step toward a more generally useful integration scheme is to clearly express our assumptions about how the CP map should be interpreted. While the pressure calculated for each voxel in the unit cell is a function of the full electronic structure of the compound, we expect that the atoms closer to a voxel will play larger roles in determining its pressure. For the purposes of interpreting the CP map in terms of pairwise interatomic interactions, we will assume that a voxel's pressure is an expression of the interaction between its two closest atoms. The involvement of other atoms in that voxel's pressure will appear as modulations to the degree of optimization of that specific interatomic interaction.

Once this assumption is articulated, a straightforward approach emerges to obtaining CP anisotropy surfaces that are reflective of the net interactions between an atom and its neighbors. We begin by dividing the unit cell into regions of space whose voxels are associated with the same interatomic contact, regions which we will refer to as *contact volumes*. We then average the pressures of the voxels within each contact volume to obtain average interatomic pressures.⁴⁷ Next, in order to evenly distribute the pressures between the atoms at each contact, the individual voxel pressures are replaced with the average pressures for their contact volumes. Finally, the voxels are assigned with a weight of one-half to both atoms of their contacts, and the projections described in the last section are carried out.

The CP anisotropy surfaces resulting from the application of this contact volume integration scheme are presented in Figure 6b, where the agreement between the semicore Ca and valence-only Ca results is substantially improved. In particular, the shapes of the positive pressure lobes along the short Ca–Ca contacts are now quite similar. Also, the placement of these black and white lobes now appears to be coordinated between the atoms. In going through the structure contact by contact, one finds that in each case the CP anisotropy surfaces on both sides of interatomic vectors are the same color. In particular, the majority of the contacts between atoms of different layers along the c -direction appear with black CP lobes. These

contacts are overly long and call for the contraction of the structure's *c*-axis. Such contraction is prevented, of course, by the strained Ca–Ca contacts within the tetrahedral chains.

The largest difference between the semicore and valence-only results is perhaps in the CP surfaces on the Sn atoms with square-antiprismatic coordination. For the semicore calculation, functions resembling d_{z^2} orbitals appear on these Sn atoms, with black lobes pointing up and down toward the Sn atoms in neighboring antiprisms, and a white torus of positive pressure directed at the surrounding Ca atoms. On moving to the valence-only result, these Sn CP anisotropy surfaces virtually vanish. In looking closely at the image, a tiny black dumbbell is barely visible at each of these sites.

This difference can be partially bridged with the application of the isotropic core component averaging procedure discussed earlier. This is shown in Figure 6c using the core radii of 0.8 and 1.3 Å for Ca and Sn, respectively. The vertical lobes of dz^2 -like surfaces for the Sn atoms in the semicore calculation have grown at the expense of the torus, leading to a surface more closely approximating a black dumbbell. Meanwhile, the black dumbbell of the valence-only calculation has grown closer to the sizes of the black lobes on the semicore result.

At this point, one could imagine making refinements on the contact volume scheme to further improve the agreement between the two choices of pseudopotentials. Indeed, the assumption that each voxel is influenced by its two closest atoms is crude in several ways. It neglects the differing sizes of atoms of different elements and has the potential to coarsely cut off the influence of other neighboring atoms that might be only slightly further out. In the newest version of our *CPintegrate* program, we have included preliminary code for a scheme in which Hirshfeld weights⁴⁸ are used in determining the relative importance of the contacts that a voxel could participate in. For Ca_5Sn_3 , this yields pictures similar to those of Figure 6c, but the option is still under development.

Even with its simplistic assumptions, the contact volume scheme offers a much clearer picture of the competing interactions within Ca_5Sn_3 than the Voronoi scheme. In the application of the DFT-CP method to a number of intermetallic phases, we have seen that these results are representative: in each case the contact volume integration scheme provides a chemically meaningful interpretation of the CP map.

CHEMICAL PRESSURE ANALYSIS OF $\text{Ca}_{36}\text{Sn}_{23}$

In the above sections, we worked through the technical details of the DFT-CP analysis and refinements to the method to improve its generality. Having built this foundation, we will now demonstrate the use of this approach in the theoretical investigation of the experimentally deduced role of size-effects in solid state structures. As a model system we will use the superstructure series based on the insertion of planar interfaces into the W_5Si_3 type (Figures 1 and 2). The driving force for such superstructure ordering was hypothesized by Corbett et al. to be the presence of overly short contacts between the larger, more electropositive atoms in the centers of the edge-sharing tetrahedra in the basic structure (Figure 3).

As a first step in exploring this idea, let us look again at the CP distribution in a hypothetical W_5Si_3 -type Ca_5Sn_3 phase, as would arise from removing the interfaces from the $\text{Ca}_{36}\text{Sn}_{23}$ or $\text{Ca}_{31}\text{Sn}_{20}$ structures. In Figure 7a, we show the LDA-DFT optimized structure of this phase (using the valence-only Ca

pseudopotential), overlaid with its atomic CP anisotropy surfaces.

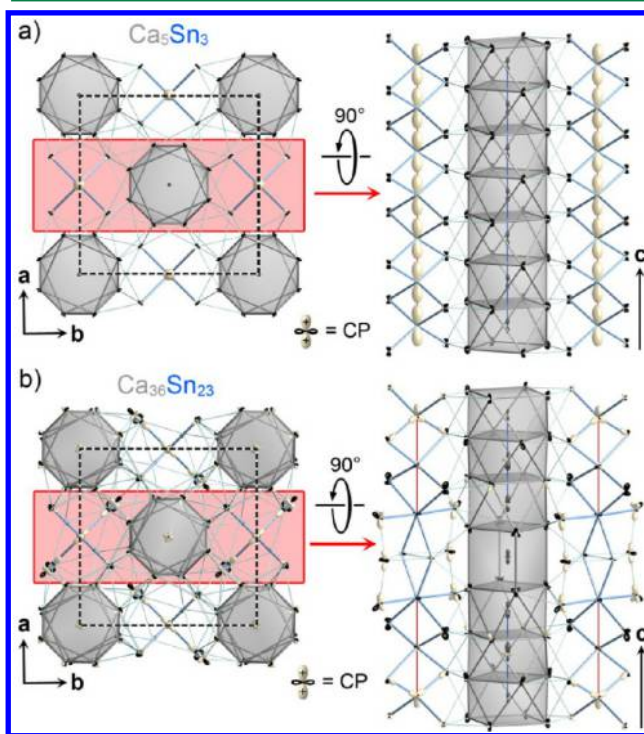


Figure 7. Comparison of the DFT-chemical pressure (CP) distributions in (a) a hypothetical W_5Si_3 -type Ca_5Sn_3 phase and (b) the observed superstructure variant $\text{Ca}_{36}\text{Sn}_{23}$. See the caption of Figure 6 for plotting conventions. The CP surfaces of panels a and b are plotted at the same scale, allowing direct comparison of their features.

For the most part, the features of the plot appear very small. The exception occurs in the chains of edge-sharing tetrahedra: for the Ca atoms at the tetrahedral centers, large white lobes are pointing up and down toward the Ca atoms in the neighboring tetrahedra (right panel). These are the largest lobes in the structure, corresponding to a positive pressure of 176 GPa. As these lobes occur along the Ca–Ca contacts in the tetrahedron chains, this suggests that the Ca–Ca distances within these chains are overly short.

Expansion of the structure to alleviate these positive pressures would then be desirable. However, such a response is prevented by the remainder of the structure, which appears decorated by small, black negative pressure features. These results confirm the model of Corbett and co-workers of the W_5Si_3 structure type being destabilized by the presence of large electropositive atoms in the tetrahedron centers.

How might the insertion of interfaces relieve these positive pressures experienced by the tetrahedrally coordinated Ca atoms? Symmetry plays a role in the CP situation of these atoms. The contacts above and below each Ca are equivalent by the mirror planes of the W_5Si_3 type's space group, $I4/mcm$. Moving upward away from the Ca atom below would increase the positive pressures along the contact above and vice versa. The insertion of a defect plane either above or below a Ca atom would break this stalemate by providing open space for the atom to move into.

In Figure 7b, we test this expectation by plotting the CP anisotropy surfaces for the $\text{Ca}_{36}\text{Sn}_{23}$ structure, in which interfaces cut the Ca_5Sn_3 structure into 3-unit-cell-thick slabs.

The right panel of Figure 7b focuses on the region near one of the interfaces. Red bars are used to connect the Ca atoms corresponding to tetrahedrally coordinated Ca atoms in the hypothetical Ca_5Sn_3 phase. Along these red bars, the vertical white lobes corresponding to Ca–Ca repulsion have essentially vanished, with the exception of those furthest from the interface at the top and bottom of the panel.

As is shown in Figure 8, a comparison of the Ca coordination environment in the tetrahedral chain in the hypothetical Ca_5Sn_3

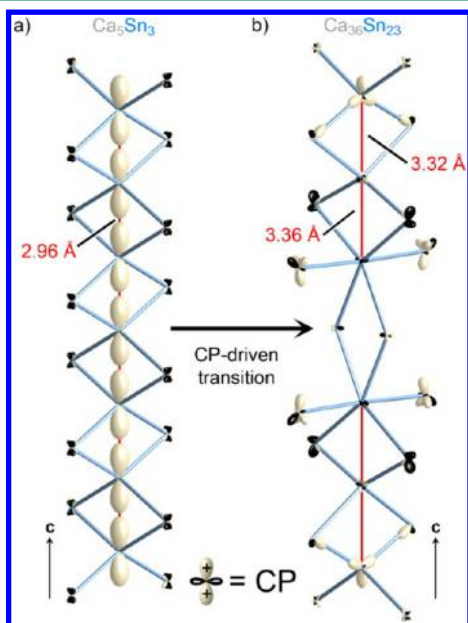


Figure 8. Chemical pressure release in the chains of Ca-centered tetrahedra on going from (a) the hypothetical W_5Si_3 -type Ca_5Sn_3 to (b) the observed structure of $\text{Ca}_{36}\text{Sn}_{23}$. Note that on going from (a) to (b) larger Ca–Ca distances are achieved by replacing edge-sharing tetrahedra with edge-sharing octahedra. As in Figure 7, the same scale is used for all CP surfaces. For plotting conventions, see the caption to Figure 6.

phase with those in $\text{Ca}_{36}\text{Sn}_{23}$ allows for this chemical pressure release to be framed in familiar chemical terms. In Ca_5Sn_3 , these atoms lie at the centers of edge-sharing tetrahedra of Sn. As is well-known from Pauling's rules,⁴⁹ shared edges between tetrahedra force the tetrahedral centers into close proximity. The tetrahedral coordination environments of large atoms are thus expected to avoid fusing at edges. It would appear that $\text{Ca}@\text{Sn}_4$ tetrahedra lie in this category.

In the corresponding regions of $\text{Ca}_{36}\text{Sn}_{23}$, a simple solution to the issue of Ca–Ca repulsion is found. Each interface bisects a Ca–Ca pair in the tetrahedral chain and places four additional Sn atoms between them. Through the incorporation of these Sn atoms, the edge-sharing tetrahedral arrangement is converted to a pair of edge-sharing octahedra. This configuration is expected to be much less sterically demanding: the ideal Sn–Ca–Sn angles in these polyhedra decrease from 109.5° in the tetrahedra to 90° in the octahedra. As a result, the polyhedral edges occur further out from the centering Ca atoms, and the Ca–Ca distances between neighboring polyhedra are substantially increased. This provides relief not only to the repulsive CPs between the Ca atoms at the interface (between which no positive CP lobe is apparent in Figure 8b) but also to the Ca atoms deeper in the W_5Si_3 -type slabs which

are free to relax toward the space provided by the octahedral Ca atoms.

In the Ca–Sn system, the appearance of planar interfaces in the W_5Si_3 type, as in $\text{Ca}_{36}\text{Sn}_{23}$ and $\text{Ca}_{30}\text{Sn}_{21}$, can thus be seen as driven by chemical pressure. The picture which emerges from this analysis confirms the insightful model of Corbett et al. for this family of superstructure phases and illustrates how DFT-CP analysis allows for the theoretical investigation and confirmation of hypotheses based on atomic size effects.

CONCLUSIONS

In this paper, we develop the idea of DFT-chemical pressure (CP) analysis into a general tool for analyzing the role atomic size has in shaping the structures of solid state materials. We described several improvements over our earlier outline of the method, including (1) the use of isotropic core component averaging to make the essential CP features in the ion core regions more apparent in the CP maps and (2) the creation of the contact volume integration scheme, in which interatomic interactions appear as mutually attractive or repulsive from the points of view of the participating atoms. The revised DFT-CP approach was then applied toward revealing the origin of the $\text{Ca}_{36}\text{Sn}_{23}$ structure, a superstructure variant of the W_5Si_3 type.

Our analysis of $\text{Ca}_{36}\text{Sn}_{23}$ confirmed the empirically derived model of Corbett et al. for this family of structures: a hypothetical W_5Si_3 -type Ca_5Sn_3 phase would have chains of edge-sharing Ca-centered Sn tetrahedra, i.e. $(\text{CaSn}_{4/2})_\infty$, which would enforce unreasonably short Ca–Ca distances. Large positive CPs occur along these Ca–Ca contacts, indicating that the distances are indeed overly short. An advantage of the DFT-CP approach is that further details can be seen in how these distances are constrained by the remainder of the structure. For $\text{Ca}_{36}\text{Sn}_{23}$, the predominant features apart from the short Ca–Ca contacts are small black lobes pointing along a variety of interactions. Such details provide clarity and precision to the useful concept of “matrix effects.”^{50–52}

The DFT-CP analysis joins a number of other theoretical tools for extracting chemical insight from electronic structure results on solid state structures. Methods in common use include the crystal orbital overlap and Hamiltonian population analyses (COOP and COHP),^{53–55} the electron localization function (ELF) and its successor, the electron localization indicator (ELI),^{56–60} and the analysis of electron density features using the quantum theory of atoms and molecules (QTAIM).^{7,8} How does the DFT-CP analysis relate to these analytical tools?

A common feature of each of the other tools listed above is that they explore the presence or strength of bonding interactions in a system with a given geometry. For example, the COHP analysis for a contact quantifies the strength of that interatomic interaction, and whether this interaction would be strengthened or weakened by a change in the electron count of the compound. Similarly an ELI analysis reveals at what points in the structure electron pairs tend to be localized, which can then be correlated with the presence of bonds or lone-pairs.

The DFT-CP analysis provides complementary information: by determining the pressures at work at each interatomic contact, it reveals to what extent the bonding strength is optimized with respect to interatomic distances. Examining the geometrical arrangements made by these pressures throughout a structure can point to where frustration arises in the optimization of these interactions and where structural transformations may be necessary. These insights may

contribute to materials design principles, growing out of a tighter integration of the roles of electronics and atomic sizes in our understanding of solid state compounds.

■ ASSOCIATED CONTENT

■ Supporting Information

A discussion on the spatial decomposition of the components of $P_{\text{remainder}}$. An annotated ABINIT input file illustrating the calculation of atomic nonlocal energies. The LDA-DFT optimized coordinates and total energies, and pressure components of $\text{Ca}_{36}\text{Sn}_{23}$ and a hypothetical W_5Si_3 -type Ca_5Sn_3 phase. This material is available free of charge via the Internet at <http://pubs.acs.org>.

■ AUTHOR INFORMATION

Corresponding Author

*E-mail: danny@chem.wisc.edu.

Notes

The authors declare no competing financial interest.

■ ACKNOWLEDGMENTS

We thank Brandon Kilduff for engaging discussions on the application of DFT-CP analysis to intermetallic phases and Yiming Guo for suggesting improvements to the code of our DFT-CP programs. We also gratefully acknowledge the financial support of the National Science Foundation (NSF) through grant DMR-1207409. This research involved calculations using computer resources supported by NSF grant CHE-0840494.

■ REFERENCES

- (1) van der Waals, J. D. *Nobel Lectures, Physics 1901–1921*; Elsevier Publishing Company: New York, 1967; pp 254–265.
- (2) Smith, M.; March, J. *March's advanced organic chemistry: reactions, mechanisms, and structure*; 6th ed.; Wiley-Interscience: Hoboken, NJ, 2007; pp 397–401.
- (3) Goldschmidt, V. M. *Trans. Faraday Soc.* **1929**, 25, 253.
- (4) Pauling, L. *J. Am. Chem. Soc.* **1927**, 49, 765.
- (5) Nolas, G. S.; Cohn, J. L.; Slack, G. A.; Schujman, S. B. *Appl. Phys. Lett.* **1998**, 73, 178.
- (6) Nolas, G. S.; Cohn, J. L.; Slack, G. A. *Phys. Rev. B* **1998**, 58, 164.
- (7) Bader, R. F. W. *Atoms in molecules: a quantum theory*; Oxford University Press: Oxford, England, 1994; pp 133–137.
- (8) Baranov, A.; Kohout, M.; Wagner, F. R.; Grin, Y.; Kniep, R.; Bronger, W. Z. *Anorg. Allg. Chem.* **2008**, 634, 2747.
- (9) Hume-Rothery, W.; Raynor, G. V. *The structure of metals and alloys*, 4th ed.; Institute of Metals: London, 1962; pp 217–245.
- (10) Laves, F. In *Theory of alloy phases; a seminar on theory of alloy phases held during the Thirty-seventh National Metal Congress and Exposition, Philadelphia, October 15 to 21, 1955*; American Society of Metals: Cleveland, 1956; pp 124–198.
- (11) Pearson, W. B. *The crystal chemistry and physics of metals and alloys*; Wiley-Interscience: New York, 1972; pp 73–79.
- (12) Simon, A. *Angew. Chem., Int. Ed. Engl.* **1983**, 22, 95.
- (13) Amerioun, S.; Häussermann, U. *Inorg. Chem.* **2003**, 42, 7782.
- (14) Mozharivskiy, Y.; Tsokol, A. O.; Miller, G. J. Z. *Kristallogr. Cryst. Mater.* **2006**, 221, 493.
- (15) Li, B.; Corbett, J. D. *Inorg. Chem.* **2007**, 46, 8812.
- (16) Xia, S.-q.; Bobev, S. J. *Am. Chem. Soc.* **2007**, 129, 10011.
- (17) Fredrickson, D. C.; Lidin, S.; Venturini, G.; Malaman, B.; Christensen, J. J. *Am. Chem. Soc.* **2008**, 130, 8195.
- (18) Fredrickson, D. C. *J. Am. Chem. Soc.* **2012**, 134, 5991.
- (19) Nielsen, O. H.; Martin, R. M. *Phys. Rev. B* **1985**, 32, 3780.
- (20) Godfrey, M. J. *Phys. Rev. B* **1988**, 37, 10176.

- (21) Ziesche, P.; Gräfenstein, J.; Nielsen, O. H. *Phys. Rev. B* **1988**, 37, 8167.
- (22) Filippetti, A.; Fiorentini, V. *Phys. Rev. B* **2000**, 61, 8433.
- (23) Rogers, C. L.; Rappe, A. M. *Phys. Rev. B* **2002**, 65, 224117/1.
- (24) Treglia, G. In *Stress and strain in epitaxy; theoretical concepts, measurements, and applications*; Elsevier Science B.V.: 2001; pp 119–150.
- (25) Gonze, X.; Rignanese, G.-M.; Verstraete, M.; Beuken, J.-M.; Pouillon, Y.; Caracas, R.; Jollet, F.; Torrent, M.; Zerah, G.; Mikami, M.; Ghosez, P.; Veithen, M.; Raty, J.-Y.; Olevano, V.; Bruneval, F.; Reining, L.; Godby, R.; Onida, G.; Hamann, D. R.; Allan, D. C. Z. *Kristallogr.* **2005**, 220, 558.
- (26) Gonze, X.; Amadon, B.; Anglade, P. M.; Beuken, J. M.; Bottin, F.; Boulanger, P.; Bruneval, F.; Caliste, D.; Caracas, R.; Cote, M.; Deutsch, T.; Genovese, L.; Ghosez, P.; Giantomassi, M.; Goedecker, S.; Hamann, D. R.; Hermet, P.; Jollet, F.; Jomard, G.; Leroux, S.; Mancini, M.; Mazevet, S.; Oliveira, M. J. T.; Onida, G.; Pouillon, Y.; Rangel, T.; Rignanese, G. M.; Sangalli, D.; Shaltaf, R.; Torrent, M.; Verstraete, M. J.; Zerah, G.; Zwanziger, J. W. *Comput. Phys. Commun.* **2009**, 180, 2582.
- (27) Leon-Escamilla, E. A.; Corbett, J. D. *Inorg. Chem.* **1999**, 38, 738.
- (28) Palenzona, A.; Manfrinetti, P.; Fornasini, M. L. *J. Alloys Compd.* **2000**, 312, 165.
- (29) Moreau, J. M.; Paccard, D.; Parthé, E. *Acta Crystallogr., Sect. B* **1976**, 32, 1767.
- (30) Cromer, D. T.; Larson, A. C. *Acta Crystallogr., Sect. B* **1977**, 33, 2620.
- (31) Fornasini, M. L.; Franceschi, E. *Acta Crystallogr., Sect. B* **1977**, 33, 3476.
- (32) Ganguli, A. K.; Guloy, A. M.; Leon-Escamilla, E. A.; Corbett, J. D. *Inorg. Chem.* **1993**, 32, 4349.
- (33) Leon-Escamilla, E. A.; Hurng, W.-M.; Peterson, E. S.; Corbett, J. D. *Inorg. Chem.* **1997**, 36, 703.
- (34) Ganguli, A. K.; Gupta, S.; Zhao, J.-T.; Alejandro Leon-Escamilla, E.; Corbett, J. D. *J. Solid State Chem.* **2005**, 178, 2959.
- (35) Kresse, G.; Furthmüller, J. *Phys. Rev. B* **1996**, 54, 11169.
- (36) Kresse, G.; Furthmüller, J. *Comput. Mater. Sci.* **1996**, 6, 15.
- (37) Monkhorst, H. J.; Pack, J. D. *Phys. Rev. B* **1976**, 13, 5188.
- (38) Vanderbilt, D. *Phys. Rev. B* **1990**, 41, 7892.
- (39) Goedecker, S.; Teter, M.; Hutter, J. *Phys. Rev. B* **1996**, 54, 1703.
- (40) Hartwigsen, C.; Goedecker, S.; Hutter, J. *Phys. Rev. B* **1998**, 58, 3641.
- (41) Momma, K.; Izumi, F. *J. Appl. Cryst.* **2011**, 41, 1272.
- (42) Fredrickson, D. C. *J. Am. Chem. Soc.* **2011**, 133, 10070.
- (43) Harris, N. A.; Hadler, A. B.; Fredrickson, D. C. Z. *Anorg. Allg. Chem.* **2011**, 637, 1961.
- (44) Martin, R. M. *Electronic structure: basic theory and practical methods*, 1st pbk. ed.; Cambridge University Press: Cambridge, UK; New York, 2008; pp 255–256.
- (45) An interesting alternative spatial resolution of the pressure was recently described in Ouahrani, T.; Menendez, J. M.; Marqués, M.; Contreras-García, J.; Baonza, V. G.; Recio, J. M. *Europhys. Lett.* **2012**, 98, 56002. Here, the focus is on the inverse of the total pressure: $1/P = -\partial V/\partial E$. The $-\partial V/\partial E$ expression is then split into a sum of volume differentials for individual atomic cells (as obtained from a QTAIM analysis) over a common ∂E denominator. Each atomic ∂V is then proportional to an inverse atomic pressure.
- (46) Okabe, A.; Boots, B.; Sugihara, K.; Chiu, S. N. *Spatial tessellations: concepts and applications of Voronoi diagrams*, 2nd ed.; Wiley: Chichester; New York, 2000; pp 43–52 and 123–127.
- (47) A relatively small group of voxels in any given structure may lie in the centers of the interstitial spaces that gives them a number of nearest neighbors at the same distance. As the number of first nearest neighbors grows beyond two, the number of contact volumes that a voxel can participate in rapidly grows. For simplicity, we treat such voxels as shared equally between its neighbors, without associating them to particular contact volumes. They are thus not included in the averaging within the contact volumes.
- (48) Hirshfeld, F. L. *Theor. Chim. Acta* **1977**, 44, 129.

- (49) Pauling, L. *J. Am. Chem. Soc.* **1929**, *51*, 1010.
- (50) Guloy, A. M.; Corbett, J. D. *Inorg. Chem.* **1996**, *35*, 2616.
- (51) Maggard, P. A.; Corbett, J. D. *Inorg. Chem.* **1998**, *37*, 814.
- (52) Maggard, P. A.; Corbett, J. D. *Inorg. Chem.* **2001**, *40*, 1352.
- (53) Hughbanks, T.; Hoffmann, R. *J. Am. Chem. Soc.* **1983**, *105*, 1150.
- (54) Hughbanks, T.; Hoffmann, R. *J. Am. Chem. Soc.* **1983**, *105*, 3528.
- (55) Dronskowski, R.; Bloechl, P. E. *J. Phys. Chem.* **1993**, *97*, 8617.
- (56) Becke, A. D.; Edgecombe, K. E. *J. Chem. Phys.* **1990**, *92*, 5397.
- (57) Savin, A.; Becke, A. D.; Flad, J.; Nesper, R.; Preuss, H.; von Schnering, H. G. *Angew. Chem., Int. Ed. Engl.* **1991**, *30*, 409.
- (58) Savin, A.; Nesper, R.; Wengert, S.; Fässler, T. F. *Angew. Chem., Int. Ed. Engl.* **1997**, *36*, 1808.
- (59) Kohout, M.; Pernal, K.; Wagner, F. R.; Grin, Y. *Theor. Chem. Acc.* **2004**, *112*, 453.
- (60) Wagner, F. R.; Bezugly, V.; Kohout, M.; Grin, Y. *Chem.—Eur. J.* **2007**, *13*, 5724.